Journal of Materials Science & Technology 249 (2026) 230–241

Contents lists available at ScienceDirect

Journal of Materials Science & Technology

journal homepage: www.elsevier.com/locate/jmst

Research Article

Micro- and nanoscale glass compression molding using the metallic glass mold

Shike Huang[a,b,c], Fei Sun[d,*], Rongce Sun[e], Lixing Zhu[a], Jinbiao Huang[a], Shengyu Zhao[a], Junsheng Liu[a], Xiangyang Yu[a], Zhiyuan Huang[e,f], Yuqiang Yan[e], Wenqiang Ruan[a], Xiaodi Liu[a,*], Jiang Ma[a,b,c,*]

[a] State Key Laboratory of Radio Frequency Heterogeneous Integration, Shenzhen University, Shenzhen 518060, China
[b] Shenzhen Key Laboratory of High Performance Nontraditional Manufacturing, Shenzhen University, Shenzhen 518060, China
[c] Guangdong Provincial Key Laboratory of Micro/Nano Optomechatronics Engineering, Shenzhen University, Shenzhen 518060, China
[d] Department of Materials Science and Engineering, Fujian University of Technology, Fuzhou 350118, China
[e] Songshan Lake Materials Laboratory, Dongguan 523808, China
[f] School of Materials Science and Engineering, Shanghai University, Shanghai 200444, China

ARTICLE INFO

Article history:
Received 24 February 2025
Revised 2 May 2025
Accepted 26 May 2025
Available online 12 July 2025

Keywords:
Microlens arrays
Glass compression molding
Metallic molds
Metallic glasses
Ir-Ni-Ta-Nb film

ABSTRACT

Glass microlens arrays (MLAs) offer flexible designability and superior light modulation capability, making them essential in optical communication, sensing, and imaging. Glass compression molding (GCM) using metallic molds is regarded as one of the most promising methods for the mass production of glass MLAs elements. However, a significant challenge lies in fabricating fine micro- and even nanostructures on the surfaces of metallic molds for GCM. To overcome this limitation, we developed a non-mechanical method that exploits the unique thermoplastic forming properties of metallic glasses (MGs). Lens arrays with structural features of 75 μm and 400 nm were successfully fabricated on the Zr-based MGs. The molded MGs were subsequently subjected to full crystallization and coated with an amorphous Ir-Ni-Ta-Nb film. This 'spawning' process yielded metallic molds suitable for the GCM process. The resulting molds demonstrated excellent anti-adhesion performance and high-temperature durability, with a surface roughness of only about 4.6 nm, and no deterioration after 30 molding cycles at 620 °C. Using these molds, corresponding glass elements were replicated with high fidelity, and their reliable imaging and focusing performance was validated. Overall, we present a convenient and promising strategy for the high-volume fabrication of precision glass elements.

1. Introduction

Glass microlens arrays (MLAs) are known for their wide field of view and infinite depth of field, exhibiting great application in imaging, beam shaping, display technologies, and optical communication [1–5]. In modern optical industries, there is a pressing need for fabricating optical elements with precise structure, versatile functions, and superior performance. The journal Science has listed "whether a perfect optical lens can be manufactured" as one of the 125 greatest scientific challenges today [6]. To date, how to manufacture micro- to nanoscale glass lens arrays with large-scale, high-precision, and low-cost, remains a hot and significant topic [7]. Although advanced fabrication techniques such as plasma etching [8], micro-milling [9], focused ion beam (FIB) milling [10], and laser-assisted micro-machining [11] have enabled the formation of micro- and nano-scale lens arrays on glass, these methods are costly, labor-intensive, and unsuitable for mass production. Fortunately, glass compression molding (GCM) enables the precise replication of micro- and nanostructured arrays from molds onto glass, characterized by high precision, enhanced manufacturing efficiency, excellent structural uniformity, and significantly reduced production costs, thus becoming a highly promising solution [12–15]. For example, G. Yang [16], K. Li [17], and F. Gong [18] successfully fabricated lens arrays with unit sizes of 60 μm, 40 μm, and 430 nm on glass surfaces using GCM, respectively. They found that increasing temperature and extending holding time significantly improved the filling ratio and shape accuracy of the lenses. Pressure also showed some effect, but its influence diminished at higher temperatures. Notably, constructing precise micro- and nanoscale optical structures on the mold surface is es-

* Corresponding authors.
E-mail addresses: sunfei2016@fjut.edu.cn (F. Sun), xdliu2018@szu.edu.cn (X. Liu), majiang@szu.edu.cn (J. Ma).

https://doi.org/10.1016/j.jmst.2025.05.073
1005-0302/

sential to the GCM process [19]. Metallic and ceramic materials are typical mold materials, including die steels [20], cemented carbides [21], WC [22], SiC [23], and sapphire [24]. The fabrication of these molds demands high-precision machining techniques, such as precision grinding [25], integrated micro-cutting and etching [26], femtosecond laser machining [27], and single-point diamond turning [28]. However, when structural dimensions fall below the hundred-micrometer scale or reach the nanometer scale, the high hardness and brittleness of these materials pose significant challenges to existing mold fabrication technologies. Utilizing single-crystal silicon (Si) templates fabricated by etching [29] and anodic aluminum oxide (AAO) templates prepared by anodization [30] enables the fabrication of structures at the hundred-nanometer scale or even smaller. Despite their advantages, these materials suffer from severe adhesion to glass at high temperatures, and their service life is limited to only a few cycles or even a single use. Therefore, developing new mold material and technologies for fabricating micro- and nano-lens arrays via GCM is of paramount importance.

Metallic glasses (MGs), also known as amorphous alloys, are a class of advanced metallic materials characterized by a long-range disordered and short-range ordered atomic structure [31–33]. Their special microstructure imparts unique thermoplastic properties distinct from crystalline alloys [34–38]. As the temperature rises into the supercooled liquid region (SLR, between the glass transition temperature T_g and the crystallization temperature T_x), the viscosity of MGs decreases by orders of magnitude with rising temperature [39]. Leveraging such property, MGs can be thermoplastically deformed into arrayed structures spanning from the macroscopic to the micro- and nano-scales [40–42], and achieve atomic-level surface roughness (Sa) [43]. It indicates that MGs can serve as highly promising cross-scale GCM mold materials, with fabricated glass elements potentially achieving extremely low Sa and thus improved optical performance. Currently, the primary obstacle is the mismatch in the T_g between the MG molds and the glass materials. The T_g of oxide glass materials usually exceeds 500 °C [44,45], whereas that of MGs generally falls below 400 °C [46–48]. Moreover, similar to other mold materials, MGs exhibit serious adhesion to glass at high temperatures [45,49]. As a result, their direct application in the GCM process has not yet been reported.

Constructing protective coatings on the mold surfaces has proven effective in improving high-temperature durability and anti-adhesion. Conventional noble metal coatings, such as Pt-Ir [50] and Ir-*Re* [44], exhibit excellent anti-adhesion properties but are rarely used in engineering fields due to their high cost. In contrast, hard nitride coatings such as TaN [51], CrN [52], and AlCrN [53] offer an optimal balance between cost and functionality. However, several significant challenges remain for these coatings, particularly concerning precise composition design and the suppression of oxidation-induced degradation. Diamond-like carbon (DLC) films have attracted considerable attention due to their exceptional nanomechanical properties and lubricating performance [54]. Nevertheless, their limited thermal stability leads to graphitization during high-temperature molding processes, resulting in premature coating peeling failure. Although α-Al_2O_3 coatings can achieve anti-adhesion with both crown glass and chalcogenide glass [45], their large grain size results in Ra of up to 100 nm, necessitating post-processing by ultra-precision grinding. Moreover, these coatings are usually susceptible to oxidation, poor wear resistance, or weak adhesion to the substrate during use, ultimately compromising mold reliability [14,55,56]. Thus, there is an urgent need for the development of new coatings and supporting strategies.

In this study, we developed an efficient strategy for fabricating micro/nano lens arrays of metallic molds with excellent high-temperature durability and anti-adhesion. The strategy leverages the superior thermoplastic forming properties of conventional MGs and a novel amorphous Ir-Ni-Ta-Nb protective coating. First, leveraging the excellent thermoplastic forming ability of Zr-based MGs, lens arrays with unit structure sizes of 75 μm and 400 nm were fabricated on their surface. The molded MGs were then annealed to a full crystalline state and coated with an amorphous Ir-Ni-Ta-Nb film, resulting in cross-scale crystallized MG (CMG) metallic molds suitable for the GCM process. With a Sa of approximately 4.6 nm, the CMG metallic mold exhibits excellent surface quality. In addition, the Ir-Ni-Ta-Nb coating not only demonstrates excellent anti-adhesion properties but also exhibits a strong adhesion force to the substrate. At 620 °C, the mold underwent 30 molding cycles without any coating peeling or glass residue, further confirming its exceptional high-temperature durability and anti-adhesion. The reliable optical performance of the fabricated glass elements was ultimately verified through imaging and focusing experiments. This study provides a convenient and efficient approach for fabricating micro/nano lens array molds, paving the way for the mass production of high–precision glass elements.

2. Experimental procedures

2.1. Materials preparation

Given the superior thermoplastic forming capability and wide SLR, the Zr-based MG $Zr_{55}Cu_{30}Ni_5Al_{10}$ (at. %) was selected for metallic mold fabrication. The reported T_g and T_x of the Zr-based MG are 411.8 and 491.8 °C, respectively [35]. The synthesized Zr-based MG was cut into circular blocks with a diameter of 10 mm. These blocks were polished using sandpaper and inlaid polishing techniques to produce a flat, mirror-like surface free of scratches. Following polishing, the physical, morphological, and roughness characteristics were determined, and are shown in Fig. S1(a–c) in Supplementary Materials, respectively. The roughness of the blocks was measured to be 2.32 nm, providing a solid basis for mold quality. The Ir-Ni-Ta-Nb MG targets were rectangular blocks, measuring 12 mm in length and 9 mm in width. Both X-ray diffraction (XRD) patterns of the Zr-based MG as well as XRD patterns of the target and the physical image after coating are shown in Fig. S2(a) and (b), respectively. The XRD patterns exhibit broad diffraction peaks, confirming that both materials are amorphous. Microlens Si templates and AAO templates were purchased from Suzhou Youzhong Micro-Nano and Shenzhen TopMembranes Technology Co., Ltd., respectively. The Si template was prepared by photolithographic reflow and etching, and the dual-channel porous AAO template was fabricated using a two-step anodization process. Fig. 1(a) shows the scanning electron microscope (SEM) image of the Si template, revealing a clean surface uniformly covered with microlenses of approximately 75 μm in diameter. The Sa results for the Si template, shown in Fig. 1(b) and (c), correspond to the areas marked R_1 (microlens top) and R_2 (platform), with Sa values of 241.8 and 287.5 pm, respectively. The excellent surface quality provides a solid foundation for the subsequent mold fabrication. The three-dimensional (3D) image of the Si template (Fig. 1(d)) indicates that the microlens structures protrude to a height of approximately 25 μm. The top-view (Fig. 1(e)) and cross-sectional (Fig. 1(f)) SEM images of the AAO template reveal uniformly distributed internal channels with diameters of approximately 300 nm. In addition, optical glass (model D-K9, Ø9 mm, 2 mm thick) with a T_g of 497 °C and a softening temperature (T_s) of 551 °C was purchased from CDGM Glass Co., Ltd., Chengdu (China). The main component of the D-K9 glass was silicon dioxide (SiO_2), with minor amounts of B, Ba, Na, and K [18].

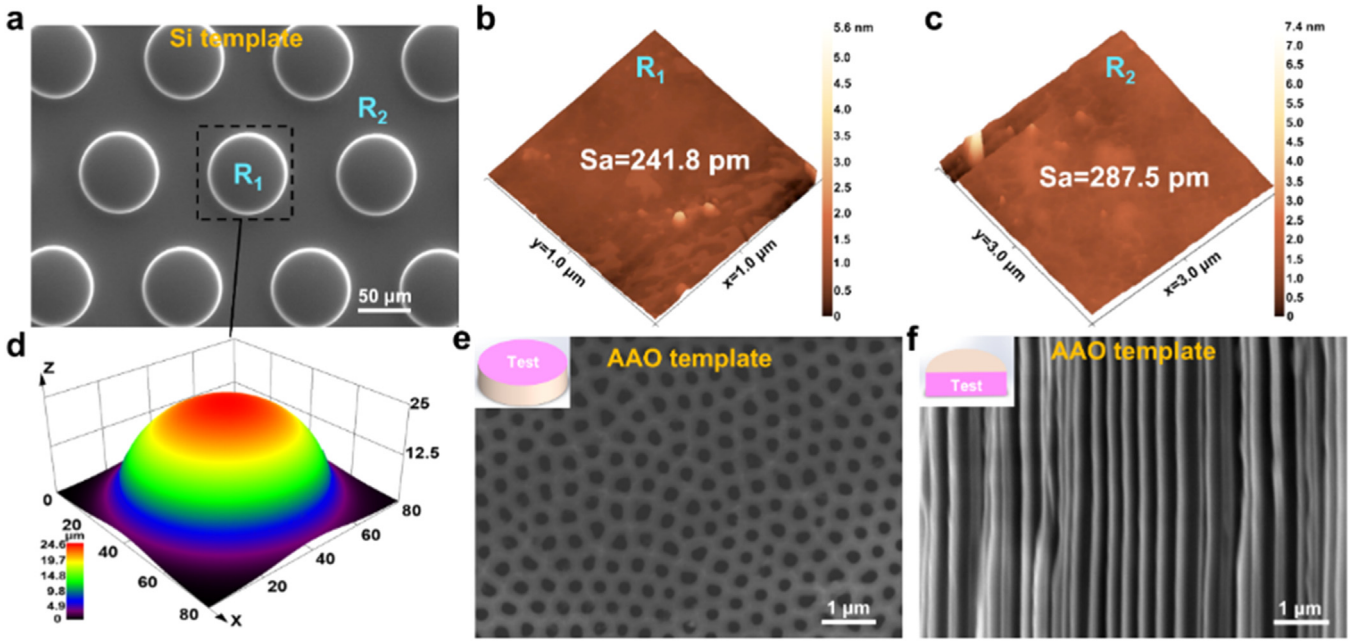

Fig. 1. Morphological characterization of precursors. (a) The SEM morphology of the Si template. (b) and (c) Roughness results for areas marked R_1 and R_2 in (a). (d) 3D structural reconfiguration diagram of the lens cell in the Si template. (e) and (f) Top-view and cross-sectional SEM images of the AAO template.

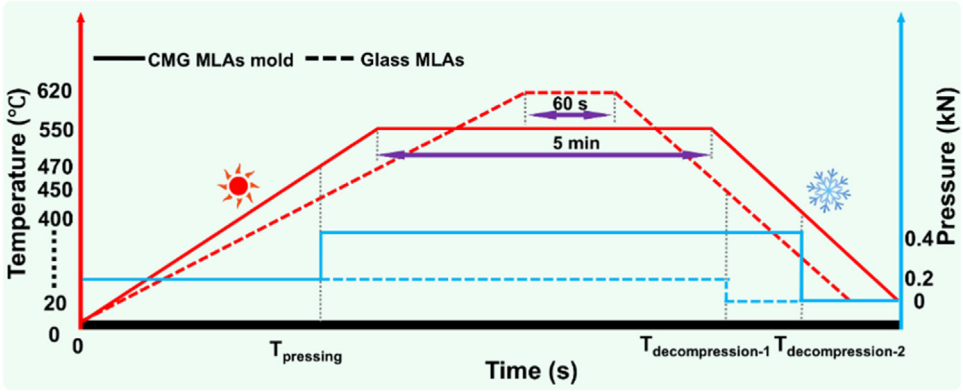

Fig. 2. Historical curve of temperature and pressure during the preparation of CMG molds with MLAs structures and glass MLAs.

2.2. Thermoplastic forming and coating

The MG and glass were shaped by thermoplastic forming using a high-vacuum MG thermoplastic forming unit (TM-YJ-03, Shenzhen University, China), which was independently developed and assembled by our research group. Both CMG molds with MLAs structures and glass MLAs were successfully prepared. Detailed temperature versus pressure history curves are shown in Fig. 2. The Zr-based MG was pre-pressed to 0.2 kN at room temperature (RT) and heated to 470 °C at 50 °C/min. A pressure of 0.4 kN was then applied and maintained, and the temperature was increased to 550 °C and held for 5 min to ensure full forming and crystallization. During the cooling stage, the pressure was applied until reaching 450 °C. The sample was cooled to RT, which completed the demolding process. In the preparation of the glass MLAs, the glass sample was heated to 620 °C at 50 °C/min, held for 1 min, and then cooled to RT. A pressure of 0.2 kN was applied from the commencement of heating to sample cooling to 400 °C. Following the thermoplastic forming, the samples were placed in a beaker filled with alcohol and subjected to vibrational demolding using an ultrasonic cleaner to generate the glass MLAs. The procedures used in the preparation of the CMG molds and the glass elements with a nano lens arrays (NLAs) structure were similar to the methods described above, with two differences during the CMG mold preparation. The applied pressure was 20 kN, with the inclusion of an additional chemical corrosion step, where the CMG molds were immersed in 1 mol/L NaOH solution to facilitate demolding. The Ir-Ni-Ta-Nb films were deposited on the CMG molds by pulsed laser deposition (PLD), using a PLD450 unit (Shenyang Scientific Instrument, Chinese Academy of Sciences). The laser emitted single pulses with an energy of approximately 500 mJ at a frequency of 2 Hz, for a deposition process time of 6 h. The DLC coating was deposited using a multifunctional vacuum composite coating system (PVD 75/90, Shenyang Weilide Vacuum Technology Co., Ltd.) at 170 °C in an argon atmosphere, with a pressure of 0.2 Pa, a current of 2.0 A, a bias voltage of −100 V, and a deposition time of 30 min.

2.3. Characterization of multi-scale structures

X-ray diffraction analysis (Rigaku MiniFlex600) was conducted to determine the amorphous or crystalline character of the Zr-based MG, Ir-based MG, and CMG. The phase structure of the deposited Ir-Ni-Ta-Nb films was confirmed by grazing incidence XRD (GIXRD, Rigaku Smartlab, Japan) using Cu Kα radiation. All the XRD analyses were conducted at a scanning rate of 2°/min

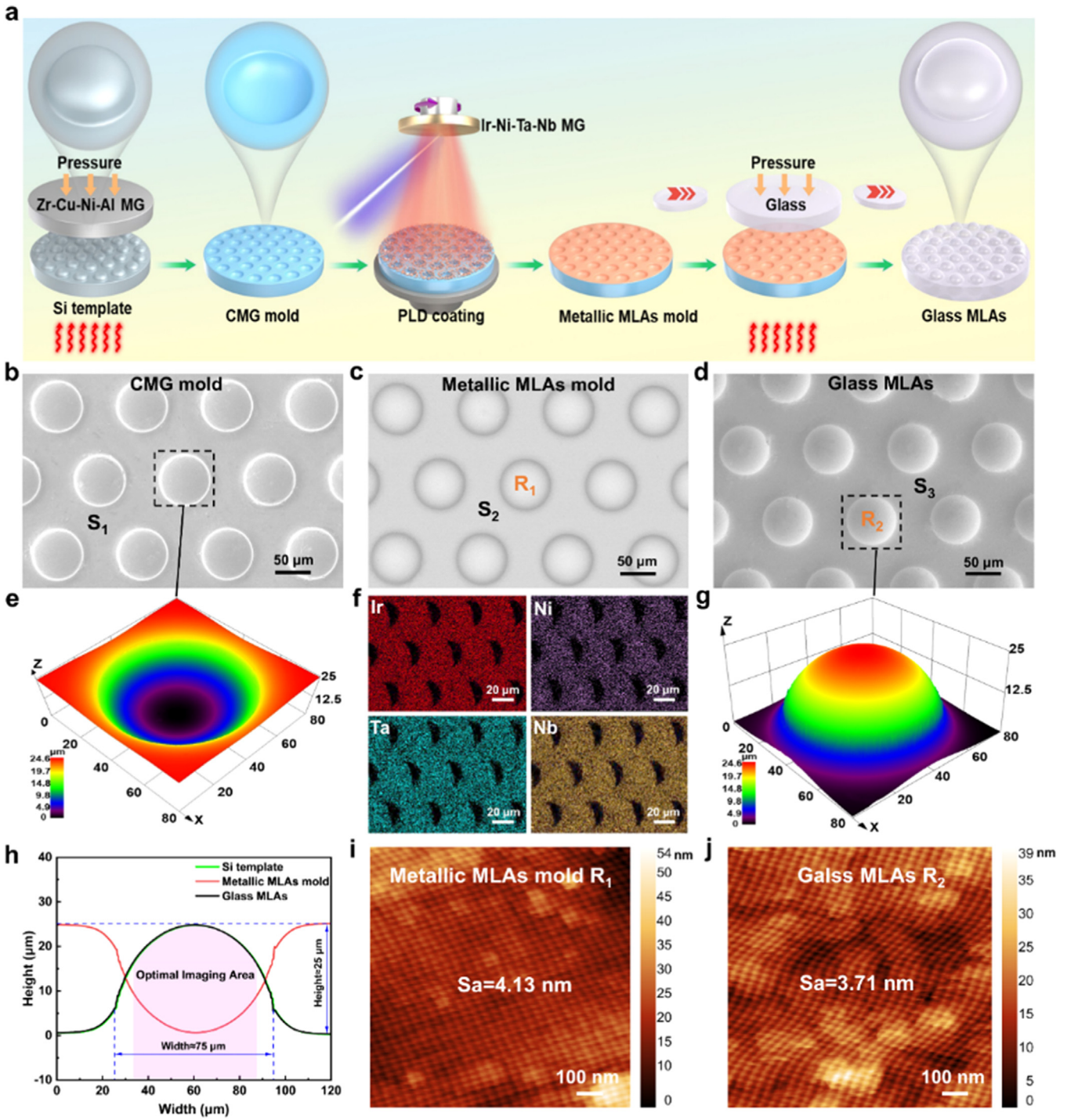

Fig. 3. Structural characterization of MLAs samples. (a) The schematic diagram for the preparation of metallic MLAs mold and glass MLAs. (b) The SEM morphology of CMG mold before coating. (c) The SEM morphology in backscattering mode of the metallic MLAs molds. (d) The SEM morphology of the glass MLAs. (e) 3D structural reconfiguration diagram of the lens cell in the CMG mold. (f) EDS results corresponding to (b). (g) Reconfiguration of 3D structure in lens units of glass MLAs. (h) Profile curves of lens units for Si templates, metallic MLAs molds, and glass MLAs. (i) and (j) Roughness of surfaces in the R_1 and R_2 regions.

over a 20°–80° 2θ range. Differential scanning calorimetry (DSC; Perkin-Elmer DSC-8000) was carried out in an argon atmosphere at 20 K/min to determine the characteristic T_g and T_x of Ir-based MG and the melting temperature (T_m) for CMG. Sample surface morphology and elemental distribution were evaluated by field-emission SEM (FEI QUANTA FEG 450). Transmission electron microscopy (TEM) measurements were made using a JEM-2100F unit (JEOL Ltd.) to determine film bonding to the substrate and atomic structure; samples were prepared using an FEI Scios SEM/FIB dual-beam system. The coefficient of thermal expansion (CTE) for CMG and Ir-based MG was measured from 20 to 800 °C using a thermo-mechanical analyzer (402 F3, NETZSCH, Germany) at a heating rate of 5 °C/min and a high-purity nitrogen atmosphere. Sample surface morphology and roughness were evaluated using an atomic force microscope (AFM, Bruker Dimension Icon, Germany). The hardness and modulus of the CMG and metallic mold surfaces were measured by nanoindentation (TI950, Hysitron). The adhesion force of the Ir-Ni-Ta-Nb and DLC films with respect to the CMG substrates was measured using a nano-scratch instrument (Klaimicro, USA) equipped with a diamond tip with a diameter of approximately

5 μm. Samples containing lens structures underwent a 3D structural reorganization using an Olympus laser confocal microscope (LEXT OLS 4500, Japan), and the profile curves were recorded. The elemental and chemical composition of the DLC coatings were analyzed by X-ray photoelectron spectroscopy (XPS; Thermo Scientific, USA) using Al Kα X-rays (characteristic energy: 1.4867 keV).

3. Results and discussion

3.1. Fabrication and morphology of the metallic MLAs mold

The schematic representation in Fig. 3(a) illustrates the process of "MLAs on glass" preparation using MG, which involves three steps. Firstly, the Zr-based MG is heated to the SLR in a vacuum chamber, pressurized to replicate the microlens structure from the Si template, and crystallized to obtain the CMG molds. Secondly, the Ir-Ni-Ta-Nb MG is used as the target, and the CMG molds are coated using PLD technology to obtain the anti-adhesive metallic MLAs molds. Thirdly, the D-K9 glass is positioned above the metallic MLAs molds and subjected to heating and pressurization in the vacuum chamber to complete the fabrication of the glass MLAs.

The morphology of the CMG mold is illustrated by the SEM image shown in Fig. 3(b) and representative low-magnification images are presented in Fig. S3(a). It can be seen that the lens units are uniformly distributed in 50 μm intervals, with no evidence of Si template residues or impurities. The morphology of the metallic MLAs molds was analyzed using SEM in backscattering mode, as shown in Fig. 3(c), and the corresponding energy disperse spectroscopy (EDS) results are presented in Fig. 3(f). Fig. S4(a) shows the physical image of the metallic MLAs molds with a diameter of 10 mm. No coating loss and localized presence of excess droplet-like material were observed in this SEM result. Additionally, the EDS results establish a uniform distribution of Ir, Ni, Ta, and Nb without any evidence of element segregation. These results confirm that the surface of each lens unit in the CMG mold is coated with an Ir-Ni-Ta-Nb film. The DSC results (Fig. S5) have established the T_m for Zr-based CMG (840 °C), and the T_g (830 °C) and T_x (948 °C) of Ir-Ni-Ta-Nb. Thus, it is confirmed that the metallic molds prepared in this work do not deform at temperatures around 800 °C. Both physical and SEM images of the fabricated 9 mm diameter glass MLA samples are shown in Figs. S4(b) and 3(d), respectively, with the lower magnification SEM images given in Fig. S3(b). The SEM images of the glass MLAs reveal a uniform distribution of the lens units with no detectable impurities, adhesion components, or structural defects, proving the anti-adhesive characteristic of the Ir-Ni-Ta-Nb coating.

The application of laser confocal microscopy served to characterize the 3D structural reconstruction of the lens units in the CMG molds and glass MLAs, as shown in Fig. 3(e) and (g). Colors in the reconstructed 3D image correspond to different heights. It can be seen that the convex microlens structure in the Si template becomes concave when copied into the CMG, and reverts to convex when replicated into the glass. The profile curves for the lens units from the Si template, metallic MLAs molds, and glass MLAs are shown in Fig. 3(h). The results reveal a lens height of 25 μm and a width of 75 μm, where the profile curves are nearly identical. Based on the profile curve of the lens unit, the morphological deviation curve was generated, as shown in Fig. S6. The peak-to-valley (PV) between the metallic MLAs mold and the glass MLAs is approximately 60 nm, which is within the acceptable PV error of 136 nm for typical microlens arrays [16]. The area shown in pink represents the main region of the lens unit used for optical imaging Fig. 3(h). The low Sa is essential for enhanced imaging quality. Analysis by AFM was performed on the areas marked as R_1 and R_2 in Fig. 3(c) and (d). The results are shown in Fig. 3(i) and (j). The Sa associated with R1 and R2 are 4.13 and 3.71 nm, respectively, satisfying the optical imaging requirement (Sa < 10 nm). The roughness results of the unstructured regions marked as S_1, S_2, and S_3 are shown in Fig. S7(a–c), respectively, with associated Sa values of 5.07, 4.74, and 4.58 nm.

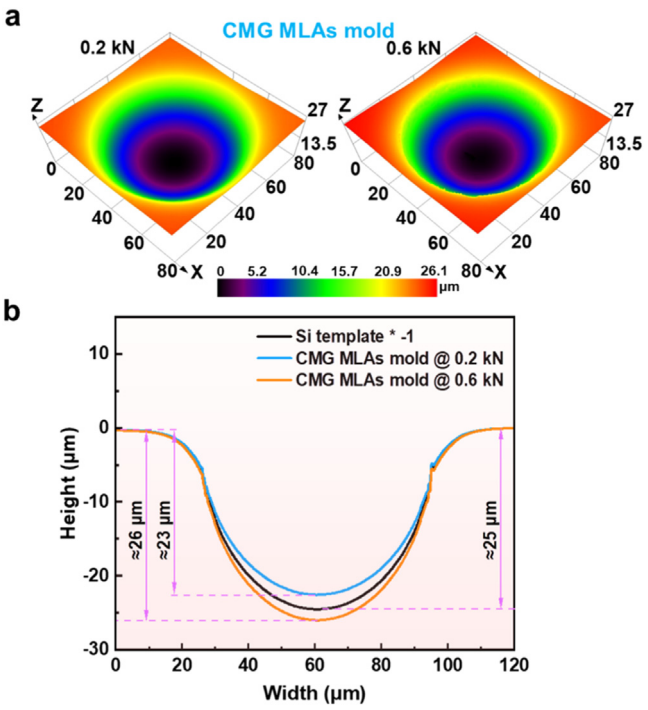

Fig. 4. Morphological characterization of CMG molds with MLAs structures fabricated under varying pressures. (a) 3D reconstructions of lens units on CMG MLAs molds fabricated under 0.2 and 0.6 kN pressures. (b) Profile curves of lens units on CMG MLAs molds fabricated under applied pressures of 0.2 and 0.6 kN.

The above-mentioned results have established a successful utilization of the thermoplastic forming property of Zr-based MG combined with novel Ir-Ni-Ta-Nb coatings to fabricate high-quality metallic molds with low roughness and anti-adhesive properties. This strategy can serve to improve the processing efficiency and quality of metallic molds for GCM with lower manufacturing costs. Furthermore, the forming quality of CMG MLAs molds under different pressures was examined. Fig. 4(a) shows the 3D structures of CMG MLAs molds fabricated at 0.2 and 0.6 kN, respectively, indicating that concave MLAs are successfully replicated under both conditions. However, there are some differences in the colors of the 3D structural images, indicating inconsistent heights following molding. Here, we extracted the associated profile curves of both, which are shown in Fig. 4(b). From the profile curves, well-formed surfaces were observed at both 0.2 and 0.6 kN, which confirms that the MG can readily mold microlens structures at this scale. It should be noted that the height at 0.2 kN is approximately 23 μm, lower than that of the Si template, which may be due to insufficient pressure. In contrast, the height at 0.6 kN reaches approximately 26 μm, exceeding the template height, which can be attributed to excessive pressure. Combining these data again demonstrates that 0.4 kN is a relatively optimal parameter.

3.2. Mechanical properties of Ir-Ni-Ta-Nb coatings

The strength of the bond between the coating and substrate is critical for practical applications, as it determines the service life of the coating and directly affects its reliability and durability in complex environments. The TEM image presented in Fig. 5(a) and EDS maps (Fig. 5(b)) serve to characterize the structure and compositional distribution of the metallic MLAs molds from a cross-

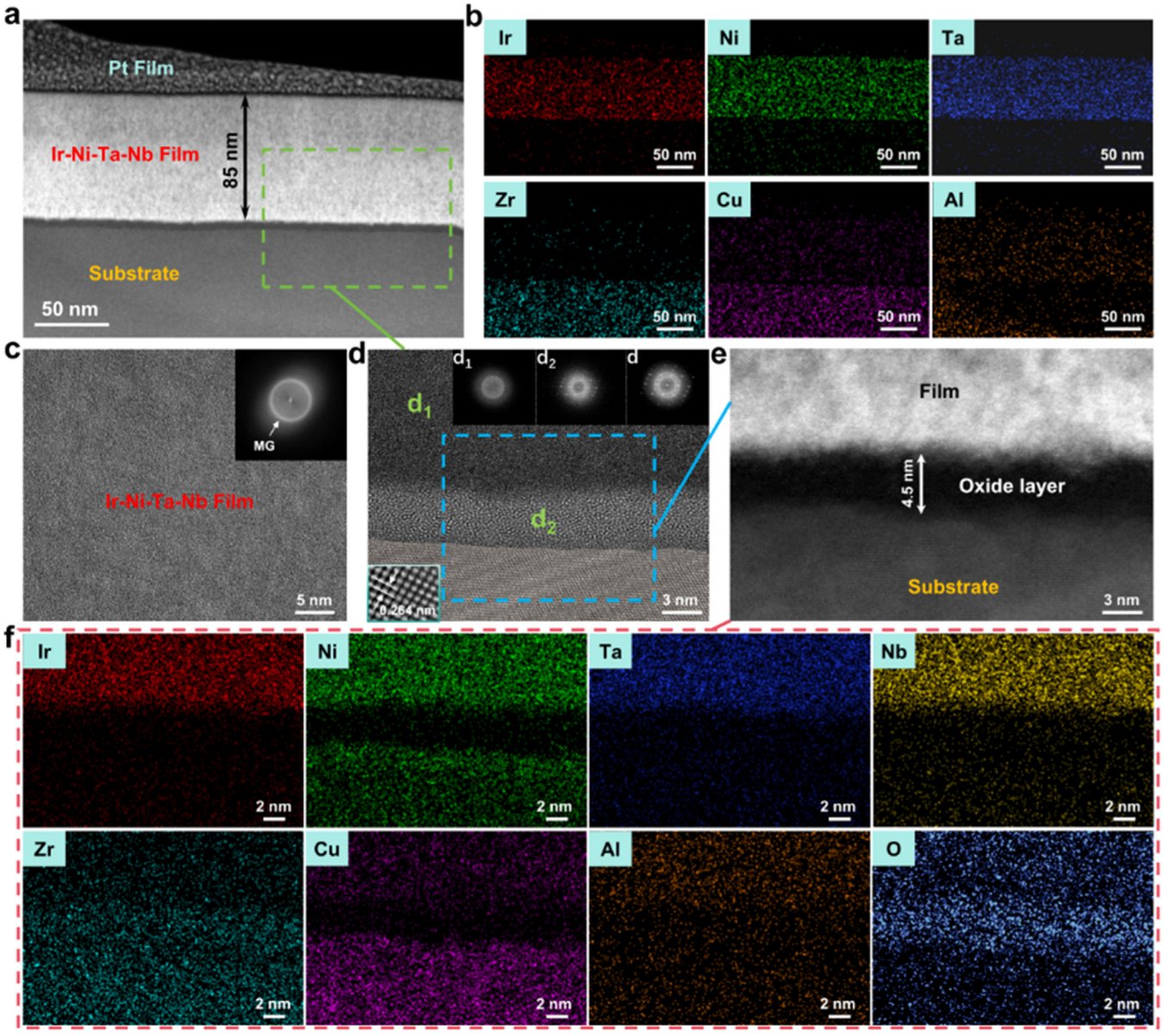

Fig. 5. Characterization results of the interface between the Ir-Ni-Ta-Nb coating and CMG molds. (a) Depicts cross-sectional TEM images of Ir-Ni-Ta-Nb films. (b) The EDS results corresponding to (a). (c) High-resolution TEM results and diffraction pattern of the Ir-Ni-Ta-Nb region. (d) High-resolution TEM results and diffractograms corresponding to the marked areas in (a). (e) HAADF imaging corresponding to the d_2 region in (d). (f) The EDS results corresponding to (e).

sectional view. It can be seen that the Ir-Ni-Ta-Nb film (85 nm thickness) is uniformly deposited on the CMG molds, where the elements exhibit a homogeneous distribution without any segregation. In Fig. 5(c), the high-resolution TEM image of the Ir-Ni-Ta-Nb film region illustrates a disordered atomic arrangement. The inset to Fig. 5(c) shows the diffraction pattern obtained by fast Fourier transform (FFT) analysis, displaying a clear diffused ring without any observable crystalline spots, which proves the amorphous structure of the film. The high-resolution TEM analysis of the area identified in Fig. 5(a) is presented in Fig. 5(d), and it can be seen that the film has formed an atomic bond with the substrate. The substrate is crystalline, characterized by an ordered atomic array with an atomic spacing of 0.264 nm. This Zr-based MG crystallization ensures structural stability, and the sample does not deform at a working temperature of approximately 800 °C. The d, d_1, and d_2 FFT diffraction analyses generate diffraction spots that confirm substrate crystallization.

The area marked in Fig. 5(d) was subjected to additional analysis by high-angle annular dark-field (HAADF) imaging (Fig. 5(e)) and EDS mapping (Fig. 5(f)). There is an ultrathin oxide layer with a thickness of 4.5 nm, which may be formed by oxidation during thermoplastic forming and exposure to the air. The EDS results suggest that the oxide layer is composed of ZrO_2. Furthermore, the analysis has revealed a partial diffusion of Zr, Cu, and Al into the film area, which may contribute to a greater bonding strength of the coating to the substrate.

In order to further research the bonding strength of amorphous Ir-Ni-Ta-Nb coatings with CMG molds, CMG plates with amorphous Ir-Ni-Ta-Nb coatings were subjected to a nano-scratch to test the adhesion. Sample morphology following the nano-scratch was observed using the backscattering mode of SEM, as shown in Fig. 6(a), where the dark gray area represents the substrate. It can be seen that the scratches gradually widen, and then stabilize. When the dark gray substrate is completely exposed, it indicates that the film has been damaged. The entire scratch testing process consists of three stages: plastic deformation, crack propagation, and penetration. Areas marked as S3, S1, and S2 in Fig. 6(a) were observed by high-magnification SEM, and the results are in

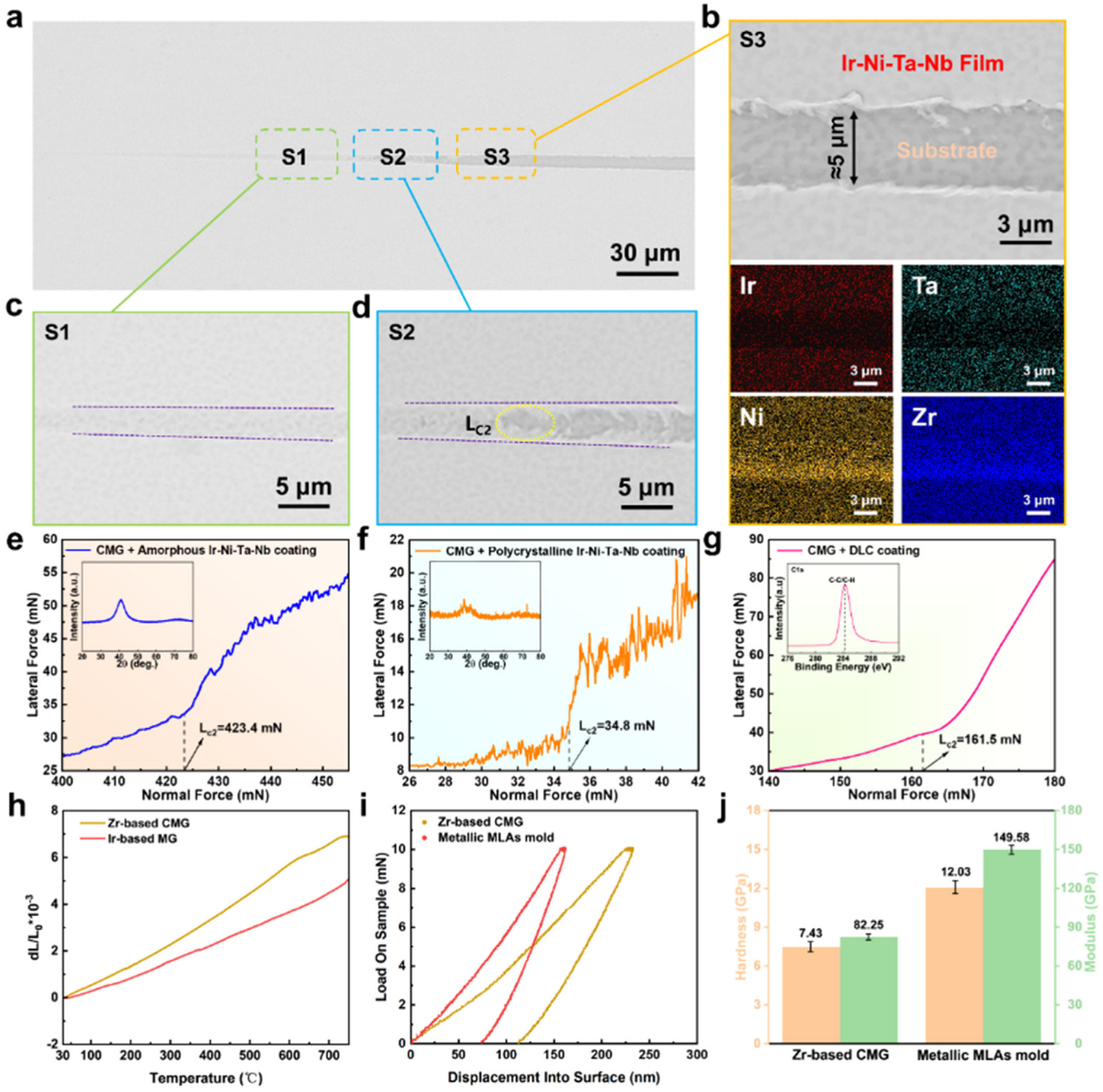

Fig. 6. Adhesion force and mechanical properties of Ir-Ni-Ta-Nb coating. (a) The SEM morphology of the CMG plate with amorphous Ir-Ni-Ta-Nb coatings after nano-scratching. (b) High-magnification SEM morphology and EDS results for the S3 region in (a). (c) and (d) High-magnification SEM morphology of the S1 and S2 regions in (a). (e) and (f) Adhesion force of amorphous and polycrystalline Ir-Ni-Ta-Nb coatings to CMG plates, along with grazing incidence XRD results. (g) DLC coating adhesion force to CMG plates and its XPS spectra. (h) Results of CTE testing from Zr-based CMG and Ir-based MG. (i) Load-displacement curves of the CMG and the metallic MLAs molds. (j) Comparison of hardness and modulus between the CMG mold and the metallic MLAs mold.

Fig. 6(b–d), respectively. The magnified image of the S1 area shows appreciable scratching as the load is increased, but the dark gray substrate is not exposed, indicating that the film is not penetrated. The magnified image of the S2 reveals a visible tear in the film, where the dark gray substrate is progressively exposed. The coating is clearly broken near the scratch edge at position L_{c2}, exposing the dark gray substrate. The magnified view of the S3 area and EDS results demonstrate that the film is fully punctured, leaving a 5 μm wide scratch without adhesion or abrasive wear, consistent with a peeling failure of the coating.

The normal force from the nano-scratch experiment was plotted against the lateral force. If the slope exhibits sudden changes, the corresponding normal force represents the critical load for coating failure (L_{c2}), which serves as a measure of the coating adhesion strength [14]. In the case of the CMG plate as a substrate, the normal force versus lateral force plots for amorphous and polycrystalline Ir-Ni-Ta-Nb coatings, and DLC coatings are shown in Fig. 6(e–g), respectively. The polycrystalline Ir-Ni-Ta-Nb coatings were obtained during the parameter optimization process using PLD at a deposition frequency of 5 Hz. The associated L_{c2} values for the coatings are 423.4, 34.8, and 161.5 mN, respectively. From the XRD patterns in the insets of Fig. 6(e) and (f), the broad diffraction peaks and the one mixed with a few crystal peaks indicate that the coatings are fully amorphous and polycrystalline, respectively. The

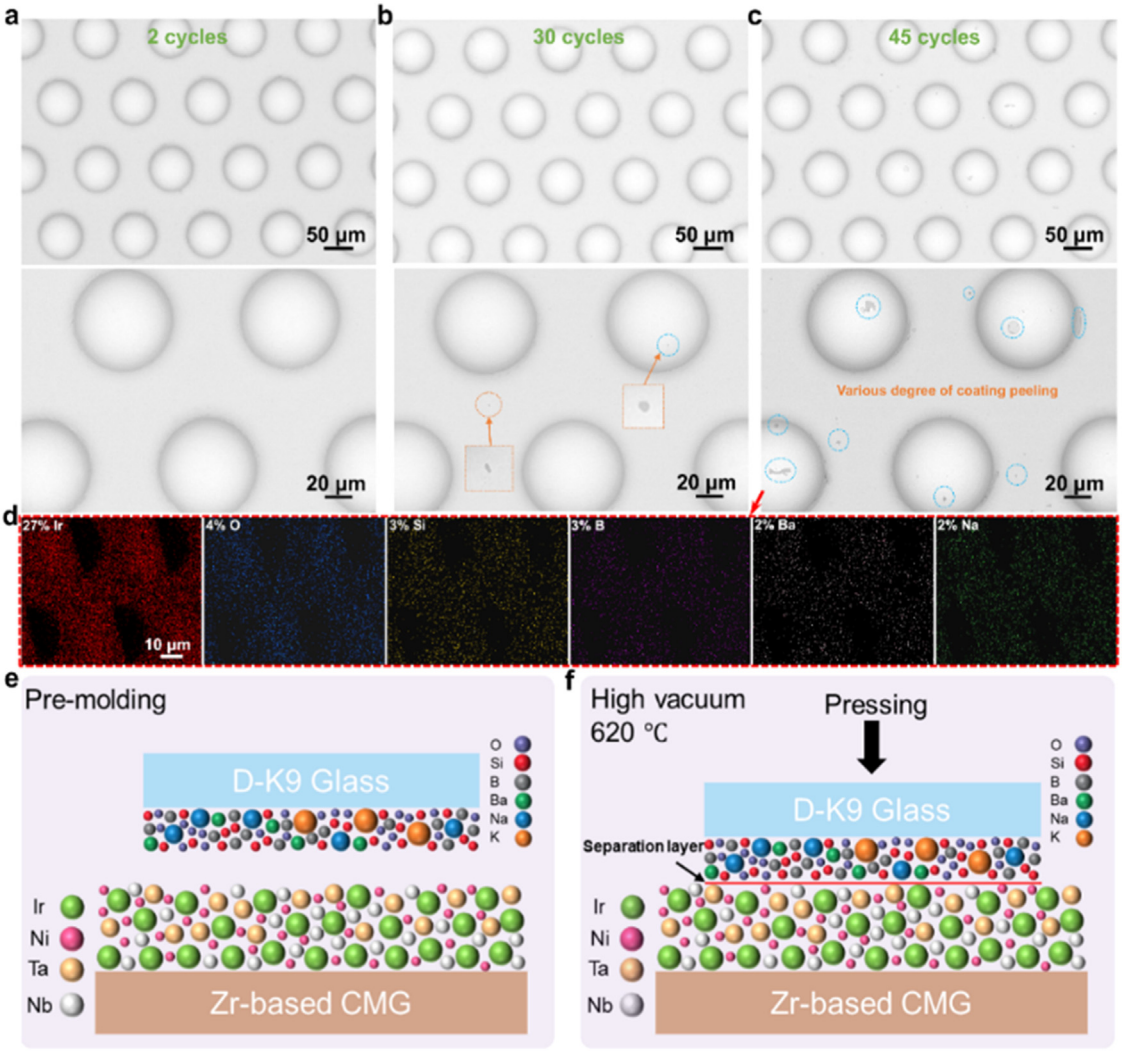

Fig. 7. Testing of anti-adhesion and repeatability between CMG metallic molds and glass. (a–c) The SEM morphology of CMG metallic molds after 2, 30, and 45 GCM cycles. (d) The EDS results correspond to the high-magnification SEM morphology in (c). (e) and (f) Schematic diagram of the anti-adhesion mechanism in CMG metallic molds for GCM before and during forming.

XPS analysis of the DLC coating shows a C1*s* peak at 284.4 eV corresponding to a graphite structure (100 % sp^2), whereas the peak at 285.0 eV is attributed to a diamond structure (100 % sp^3) [57]. Also, the broad peak at 284.7 eV indicates the presence of amorphous carbon, which confirms the DLC structural features of the films and its corresponding fitted spectrum is presented in Fig. S8. Applying the ratio of sp^2 to sp^3 C-C obtained from the Gaussian fitting of the C1*s* energy spectrum, the calculated sp^2/sp^3 value is 2.59. Consequently, the amorphous Ir-Ni-Ta-Nb coating exhibits a stronger adhesion force when compared with the polycrystalline Ir-Ni-Ta-Nb and the commercial DLC coatings. Moreover, a favorable result was obtained in this study when compared to the usual 80 mN adhesion force [14].

A suitable match of the substrate and coating CTE is crucial to prevent the peeling of the coating during repeated use and maintain the precision of the microstructure. The linear CTE was calculated using Eq. (1):

$$\alpha = \frac{\Delta L}{L_0 \Delta T} \tag{1}$$

where L_0, ΔL, and ΔT denote the initial length, elongation, and change in the temperature of the sample, respectively [35].

Fig. 6(h) presents the CTE curves of Zr-based CMG and Ir-based MG. The calculated CTE over the temperature range of 30–750 °C for the two materials is 9.51 and 7.08 ppm/K. The CTE values are similar, do not exceed 10 ppm/K, and both materials can be considered to exhibit constant expansion properties. Fig. 6(i) and (j) illustrates the nanoindentation results of CMG and metallic MLAs molds. The hardness and modulus of the surface of CMG molds coated with amorphous Ir-Ni-Ta-Nb film increase from 7.43 to 12.03 GPa and from 82.25 to 149.58 GPa, respectively. Surfaces exhibiting a high hardness and modulus enable the molds to resist microstructure deformation under load, just as the indentation depth of metallic MLAs molds is shallower than CMG molds.

Overall, the amorphous Ir-Ni-Ta-Nb coating improves the mechanical properties of Zr-based CMG surfaces, exhibiting excellent bonding quality to the substrate. Suffice it to believe that the quality and durability of the mold will benefit from these properties.

3.3. Anti-adhesion and repeatability of the CMG metallic mold

Most sticking phenomena associated with the GCM involve the glass adhering to the surface of the mold, where the anti-sticking coating peels off after many cycles of GCM. Therefore, the morphology of the metallic MLAs molds after many GCM cycles was investigated by SEM in backscattering mode, with the results shown in Fig. 7(a–c). Following 2 and 30 cycles of GCM, it can be seen that there are no black glass adhesions on the surface of the

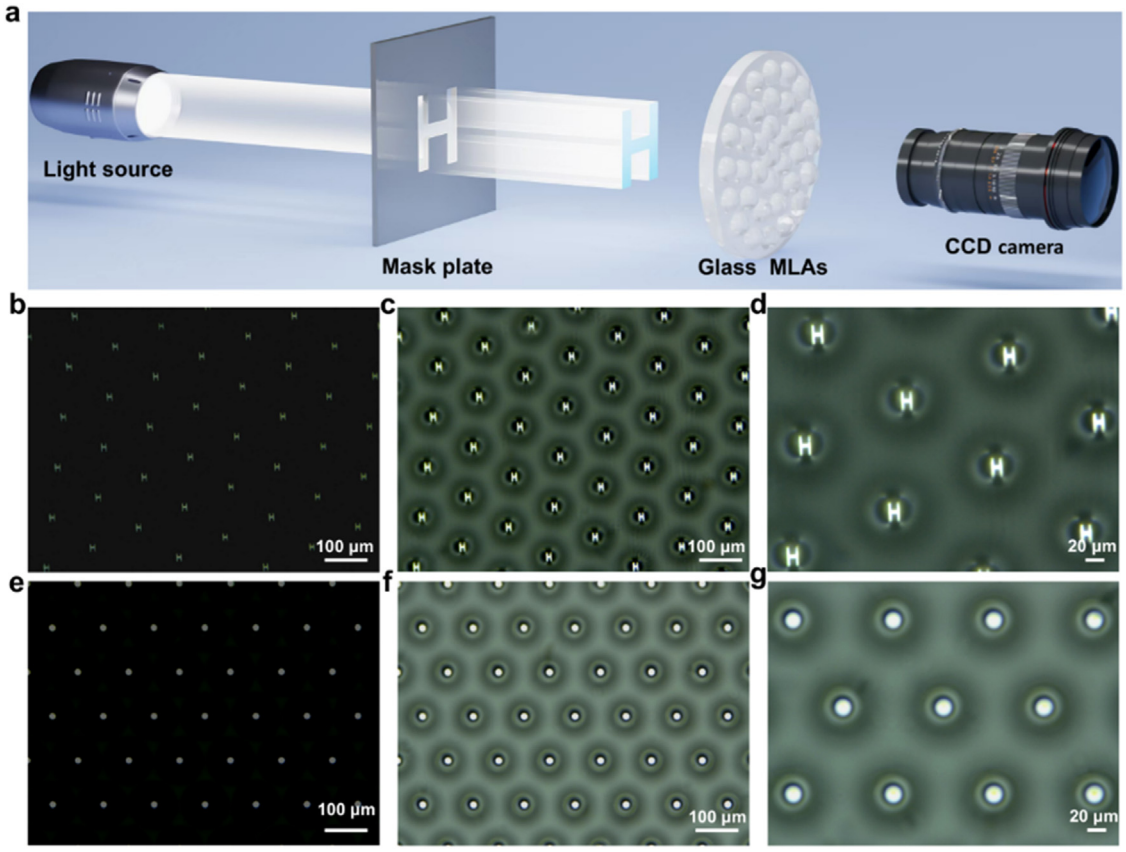

Fig. 8. Characterization of imaging and focusing properties of glass MLAs. (a) Schematic diagram of the test for optical properties. (b) Glass MLAs in dark-field imaging H-word results. (c) and (d) The results of different magnifications for observing glass MLAs imaging H-word in a bright field. (e) Results of dark-field focusing in glass MLAs. (f) and (g) Different magnifications to observe the results of glass MLAs in bright field focusing.

mold, which proves that the amorphous Ir-Ni-Ta-Nb coating exhibits excellent anti-adhesion properties and stability. In the high-magnification SEM images of the mold after 2 cycles, the surface appears intact, without any exposure of substrate, or evidence of coating peeling. In contrast, the high-magnification SEM image of the mold after 30 cycles reveals two areas of exposed dark gray substrate, approximately 1 μm in size, indicating slight peeling of the coating. As the number of cycles increases, the regions of peeling grow in number and area. The SEM results of the mold after 45 cycles reveal various degrees of coating peeling from in the mold. Most of these peeled regions are 3–5 μm and appear randomly at the bottom and edges of the lens unit, and the unstructured platform area. Taken together, these results indicate that the coating fails in a progressive manner. Each GCM cycle results in localized tearing and thermal stress in the coating, leading to the formation of micro-cracks in the film. These micro-cracks subsequently expand, interconnect, and ultimately cause the coating to fail by physical peeling. Notably, the repeatability of the molds in this study is excellent compared to most molds reported, which suffer from coating peeling of hundreds of microns or even visible to the naked eye after around 10–20 cycles. Furthermore, the cycling experiments have demonstrated that the molds in this study can withstand at least 30 GCM cycles without any coating peeling. It is anticipated that increasing the coating thickness or adding transition layers will significantly enhance the durability of the mold.

Fig. 7(d) corresponds to the EDS results of high-magnification SEM of the mold after the 45th GCM cycle, where 27 % Ir and 4 % O indicate that the coating possesses excellent antioxidant performance. Meanwhile, this result proves that the coating inevitably reacts chemically with oxygen during the GCM cycle. Additionally, the Ir-dominant elements in the coating do not extend to the glass. The content of Si (3 %), B (3 %), Ba (2 %), and Na (2 %) is relatively low, confirming that the glass elements do not spread to the mold surface. Therefore, the EDS results further confirm the excellent anti-adhesion properties of the Ir-Nb-Ta-Nb coatings. The schematic diagrams presented in Fig. 7(e) and (f) illustrate the anti-adhesion mechanism during the GCM process, both before and during the forming process under a vacuum at 620 °C. Before forming, the surface of the mold prepared with the Zr-based CMG is covered with an amorphous Ir-Ni-Ta-Nb coating, while a number of elements (O, Si, B, Ba, Na, and K) are dispersed on the D-K9 glass surface. In the forming under vacuum at 620 °C, a separation layer between the Ir-Ni-Ta-Nb coating and glass surface prevents diffusion of the main elements, resulting in superior anti-adhesion properties [49].

3.4. Optical properties of the glass MLAs

The optical performance of the glass MLAs is a critical factor in evaluating the effectiveness of the proposed strategy [1,12]. To this end, the imaging and focusing capabilities of the glass MLAs were systematically assessed using the experimental setup illustrated in Fig. 8(a). A light source was used to illuminate a mask plate engraved with the letter "H" producing an H-shaped light beam that impinged on the bottom of the glass MLAs sample. Subsequently, a charge-coupled device (CCD) camera was employed to capture the imaging effects on the structured surfaces of the glass MLAs samples. Dark-field imaging (Fig. 8(b)) has revealed a uniformly distributed bright H-shaped pattern on the surface with sharp contours. The bright-field images at low (Fig. 8(c)) and high (Fig. 8(d)) magnifications clearly show the uniform distribution of lens structures. Notably, the bright H-shape appears at the top and

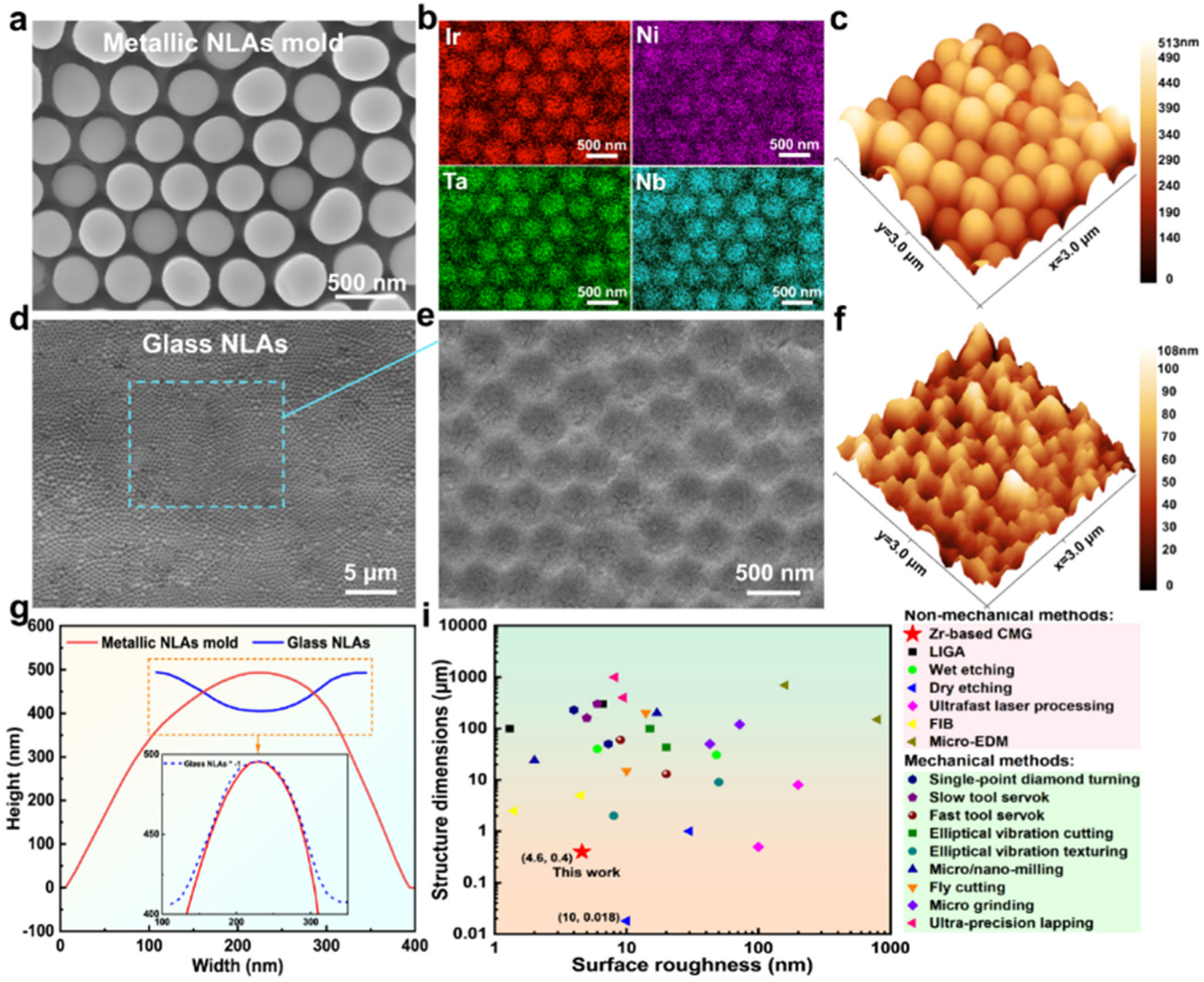

Fig. 9. Morphological characterization of samples with NLAs. (a) The SEM morphology of metallic NLAs mold. (b) Corresponding to the EDS results of (a). (c) Results of AFM from metallic NLAs mold. (d) and (e) Different magnification SEM morphology of glass NLAs. (f) The AFM characterization of glass NLAs. (g) Profile curves of lens units in samples with NLAs. (i) Comparison between roughness and structural dimensions of optical molds fabricated by different technologies.

center of each lens unit, demonstrating the superior imaging quality. When the mask plate was removed and the light source directly projected onto the glass MLAs samples, the focusing performance was captured using the CCD camera. The dark-field focusing results (Fig. 8(e)) exhibit luminous dots approximately 15 μm in diameter uniformly distributed on the surface. In the bright field, luminous dots are also uniformly distributed and centered at the top of the lens unit, as shown in Fig. 8(f) and (g). The outstanding optical performance of the glass MLAs in bright- and dark- fields demonstrates the potential of this strategy for optical applications.

3.5. Fabrication of glass elements featuring NLAs

When the structural size of the MLAs reduces to submicron and even nanoscale (i.e., NLAs), there may be more fascinating and versatile applications in the field of optics [2]. Hence, the feasibility of applying the proposed strategy to fabricating glass elements with nanostructures was further investigated. Interestingly, the metallic NLAs mold and glass NLAs were successfully prepared. The CMG molds were initially prepared using AAO templates, and the surface of the molds was coated with the amorphous Ir-Ni-Ta-Nb film to obtain metallic NLAs molds. Both SEM morphology and EDS results of this mold are shown in Fig. 9(a) and (b). It can be observed that lens structures with a diameter of approximately 400 nm are uniformly distributed on the surface. Additionally, the uniform distribution of Ir, Ni, Ta, and Nb elements without segregation demonstrates that the mold is successfully coated with the Ir-Ni-Ta-Nb film. As shown in Fig. 9(c), the 3D structure of the mold obtained from AFM analysis displays raised lens structures with a height that was almost consistent. The morphology of the glass NLAs obtained from SEM measurements is shown in Fig. 9(d) and (e). The surface of this element features a uniform distribution of concave lens structures with a diameter of approximately 200 nm. Fig. 9(f) illustrates the 3D structure of the elements obtained by AFM. It can be seen that the majority of the lenses are consistent in depth. As shown in Fig. 9(g), the profile curves of the lens units for both molds and elements are depicted. The height of a lens unit on the mold is approximately 500 nm, while the depth of the counterpart on the element is approximately 90 nm. Flipping the profile of the element, as shown in the inset of Fig. 9(g), results in a near overlap with the profile of the mold, demonstrating that the strategy is highly effective. In the future, it will be possible to fabricate various high-quality glassy elements featuring nanostructures based on the optimization of the thermoplastic forming process.

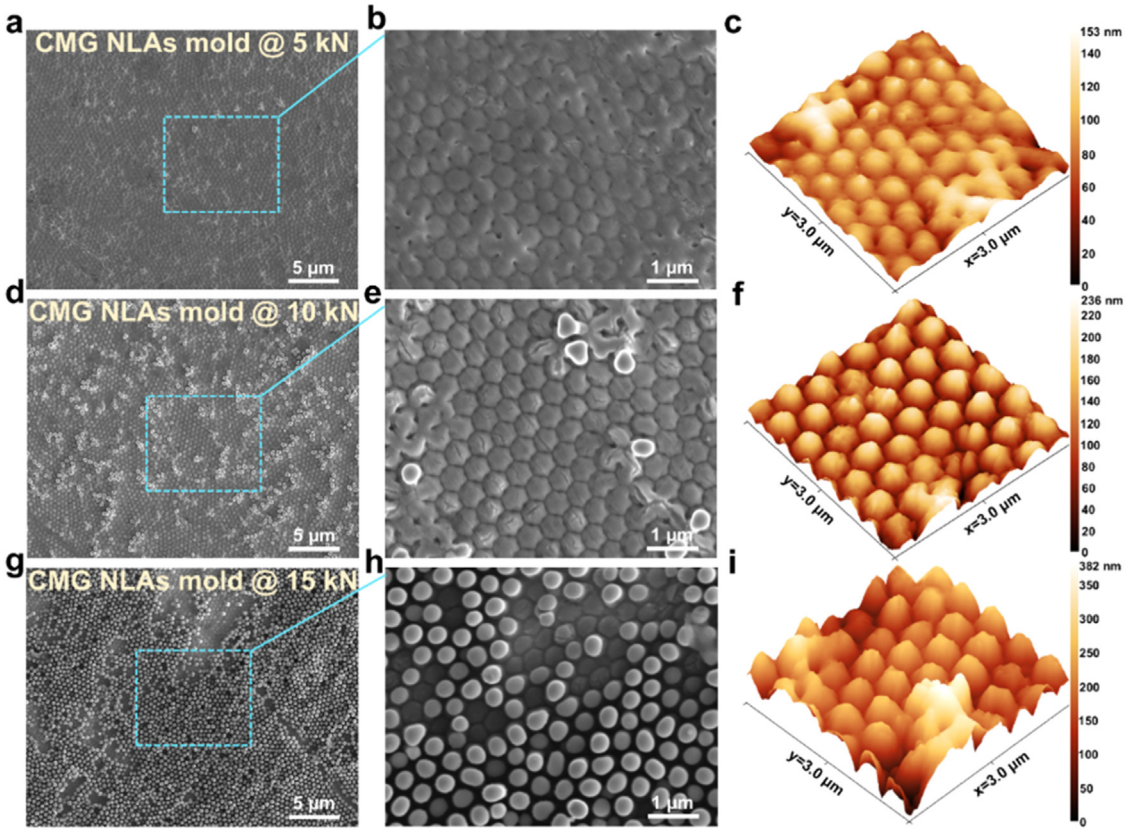

Fig. 10. Morphological characterization of CMG molds with NLAs structures fabricated under varying pressures. (a) and (b) The SEM images at different magnifications of the CMG NLAs mold fabricated under 5 kN. (c) Results of AFM from the CMG NLAs mold @ 5 kN. (d) and (e) Different magnification SEM morphology of the CMG NLAs mold prepared under 10 kN. (f) The AFM results correspond to the CMG NLAs mold @ 10 kN. (g) and (h) The SEM morphology at different magnifications of the CMG NLAs mold obtained under 15 kN. (i) The AFM analysis results of the CMG NLAs mold @ 15 kN.

Current methods of manufacturing GCM molds can be divided into mechanical and non-mechanical procedures. Sa and the structural dimensions of GCM molds prepared using different processing techniques are summarized in Fig. 9(i), and the pertinent data are given in Table S1. As can be found, the Sa and structural dimensions of the molds prepared in this work are 4.6 nm and 400 nm, which are superior to that reported for the majority of methods. The excellent result achieved is closely related to the high quality of the precursor. Most importantly, the excellent thermoplastic forming capability of MG enables high-quality replication of micro- and nano-scale structures from the precursor under appropriate processing conditions, achieving complete structural transfer while preserving superior surface quality. This is a capability that traditional metallic materials inherently lack. Moreover, conventional fabrication methods for micro- and nanostructures, such as mechanical cutting and laser engraving, tend to generate significant debris and heat, making it difficult to achieve fine structural features and low Sa. The structural dimension of the mold prepared by dry etching is 18 nm, indicating that the method can provide an excellent precursor for the proposed strategy. Above all, the strategy in this work breaks through the conventional limitations associated with the structural dimension of metallic materials, paving the way for the large-scale preparation of glass elements with diverse structures.

In addition, we conducted a detailed evaluation of the forming quality of CMG NLAs molds fabricated under different pressures. As shown in Fig. 10(a) and (b), shallow circular nanostructures are uniformly distributed on the mold surface under an applied pressure of 5 kN. Fig. 10(c) presents the AFM results of the mold fabricated under 5 kN, showing that the protrusion height of these structures is approximately 150 nm. Increasing the pressure to 10 kN resulted in a uniform distribution of shallow hexagonal nanostructures on the mold surface (Fig. 10(d) and (e)), with a limited number of protruding nanopillars. The corresponding AFM results are shown in Fig. 10(f), indicating that the protrusion height is approximately 220 nm. A further increase in pressure to 15 kN (Fig. 10(g) and (h)) results in numerous protrusions uniformly distributed on the mold surface, and shallow circular nanostructures remain in some regions. As shown in Fig. 10(i), the AFM analysis has revealed a protrusion height of approximately 350 nm. The research findings demonstrate a clear positive relationship between the applied pressure and the resulting protrusion height of the molded structures. Moreover, the findings reinforce that a pressure of 20 kN represents the optimal condition for CMG NLAs mold fabrication, yielding a superior molding quality.

4. Conclusions

This study presents an innovative strategy for the fabrication of cross-scale lens array metallic molds with excellent high-temperature tolerance. Two typical lens array molds were successfully prepared, featuring structural units of 75 μm and 400 nm, respectively, with a Sa of approximately 4.6 nm. The fabricated CMG metallic molds demonstrated superior high-temperature resistance and anti-adhesion properties, with no evidence of coating delamination and glass residues after 30 molding cycles at 620 °C. Furthermore, the reliable optical performance of the prepared glass elements was validated in imaging and focusing tests. Our research findings establish a simple and efficient methodology for the scal-

able production of high-precision MLAs molds, paving the way for the large-scale manufacture of advanced glass optical components.

Declaration of competing interest

The authors declare that they have no known competing financial interests or personal relationships that could have appeared to influence the work reported in this paper.

CRediT authorship contribution statement

Shike Huang: Writing – review & editing, Writing – original draft, Visualization, Validation, Methodology, Investigation, Formal analysis, Data curation, Conceptualization. **Fei Sun:** Writing – review & editing, Project administration, Investigation. **Rongce Sun:** Supervision, Methodology, Investigation, Data curation. **Lixing Zhu:** Supervision, Methodology, Investigation, Data curation. **Jinbiao Huang:** Supervision, Methodology, Investigation, Data curation. **Shengyu Zhao:** Supervision, Methodology, Investigation, Data curation. **Junsheng Liu:** Supervision, Methodology, Investigation, Data curation. **Xiangyang Yu:** Supervision, Methodology, Investigation, Data curation. **Zhiyuan Huang:** Supervision, Methodology, Investigation, Data curation. **Yuqiang Yan:** Supervision, Methodology, Investigation, Data curation. **Wenqiang Ruan:** Supervision, Methodology, Investigation, Data curation. **Xiaodi Liu:** Writing – review & editing, Project administration, Investigation. **Jiang Ma:** Writing – review & editing, Supervision, Resources, Investigation.

Acknowledgements

The work was financially supported by the Key-Area Research and Development Program of Guangdong Province (No. 2024B0101070001), the NSF of China (Grant Nos. 52371160, 52401217, 52271150, 52201185, and 52201186), the Applied Research Program of Guangdong Province (No. 2019B030302010), the Science and Technology Innovation Commission Shenzhen (Nos. RCJC20221008092730037 and 20220804091920001), and the Fujian University of Technology Foundation (No. GY–Z24019). Additionally, this project is supported by the Special Fund for the Cultivation of Independent Innovation Achievements of Postgraduate Students at Shenzhen University (No. 315–000066010722). We thank the Instrumental Analysis Center of Shenzhen University for the assistance with the Electron Microscope.

Supplementary materials

Supplementary material associated with this article can be found, in the online version, at doi:10.1016/j.jmst.2025.05.073.

References

[1] A. Arbabi, A. Faraon, Nat. Photonics 17 (2022) 16–25.
[2] S. Kacker, K.L. Cahoy, Opt. Eng. 62 (2023) 113106.
[3] A. Ünal, J. Opt. 52 (2022) 956–968.
[4] E. Tseng, S. Colburn, J. Whitehead, L. Huang, S.-H. Baek, A. Majumdar, F. Heide, Nat. Commun. 12 (2021) 6493.
[5] S.I. Bae, K. Kim, K.W. Jang, H.K. Kim, K.H. Jeong, Adv. Opt. Mater. 9 (2021) 2001657.
[6] D. Kennedy, C. Norman, Science 309 (2005) 75.
[7] T.F. Zhou, X. Liu, Z. Liang, Y. Liu, J. Xie, X. Wang, Front. Mech. Eng. 12 (2017) 46–65.
[8] M.J. Ahamed, D. Senkal, A.A. Trusov, A.M. Shkel, J. Microelectromech. Syst. 24 (2015) 790–800.
[9] M. Arif, M. Rahman, W.Yoke San, Int. J. Mach. Tools Manuf. 51 (2011) 170–181.
[10] S. Gorelick, A. De Marco, Opt. Express 26 (2018) 13647–13655.
[11] C.K. Chung, S.L. Lin, H.Y. Wang, T.K. Tan, K.Z. Tu, H.F. Lung, Appl. Phys. A 113 (2013) 501–507.
[12] Q. Huang, Q. Jia, J. Feng, H. Huang, X. Yang, J. Grenzer, K. Huang, S. Zhang, J. Lin, H. Zhou, T. You, W. Yu, S. Facsko, P. Jonnard, M. Wu, A. Giglia, Z. Zhang, Z. Liu, Z. Wang, X. Wang, X. Ou, Nat. Commun. 10 (2019) 2437.
[13] G. Yang, K. Yang, J. Li, C.F. Cheung, F. Gong, Precis. Eng. 91 (2024) 587–600.
[14] C. Shu, S. Yin, S. Huang, Ceram. Int. 50 (2024) 5210–5223.
[15] C. Shu, S. Yin, Y. Li, Z. Mao, X. Guo, S. Huang, Ceram. Int. 48 (2022) 15800–15810.
[16] L. Li, G. Yang, W.B. Lee, M.C. Ng, K.L. Chan, Appl. Surf. Sci. 500 (2020) 144004.
[17] K. Li, X. Huang, Q. Chen, G. Xu, Z. Xie, Y. Wan, F. Gong, J. Manuf. Process. 57 (2020) 469–476.
[18] F. Gong, G. Lian, Z. Wang, K. Li, Mater. Des. 233 (2023) 112278.
[19] T.F. Zhou, Y.P. He, T.X. Wang, Z.C. Zhu, R.Z. Xu, Q. Yu, B. Zhao, W.X. Zhao, P. Liu, X.B. Wang, Int. J. Extreme Manuf. 3 (2021) 042002.
[20] Q.P. He, J. Xie, R.B. Guo, P.X. Ma, Y.J. Lu, Mach. Sci. Technol. 22 (2018) 1029–1044.
[21] H. Tong, Y. Li, L. Zhang, J. Micromech. Microeng. 28 (2018) 025013.
[22] S.D. Sun, K.S. Li, W.Y. Chu, F. Gong, Int. J. Refract. Met. Hard Mater. 105 (2022) 105841.
[23] Y.C. Pan, Q.L. Zhao, B. Guo, B. Chen, J.H. Wang, X.Q. Wu, Int. J. Mech. Sci. 170 (2020) 105351.
[24] M. Yoshimoto, Appl. Phys. A 121 (2015) 321–326.
[25] B. Guo, Q. Zhao, M.J. Jackson, Int. J. Adv. Manuf. Technol. 64 (2012) 727–735.
[26] T. Zhou, R. Xu, B. Ruan, Z. Liang, X. Wang, Precis. Eng. 54 (2018) 314–320.
[27] Z. Chen, H. Yuan, P. Wu, W. Zhang, S. Juodkazis, H. Huang, Opt. Lett. 47 (2022) 22–25.
[28] L. Zhang, N.J. Naples, W.C. Zhou, A.Y. Yi, J. Micromech. Microeng. 29 (2019) 065004.
[29] J. Albero, L. Nieradko, C. Gorecki, H. Ottevaere, V. Gomez, H. Thienpont, J. Pietarinen, B. Päivänranta, N. Passilly, Opt. Express. 17 (2009) 6283–6292.
[30] X. Liu, K. Li, J. Shen, F. Gong, Ceram. Int. 47 (2021) 18367–18375.
[31] A.L. Greer, Science 267 (1995) 1947–1953.
[32] S.Y. Liang, L.T. Zhang, Y.J. Wang, B. Wang, J.M. Pelletier, J.C. Qiao, Int. J. Fatigue 187 (2024) 108446.
[33] S.Y. Liang, F. Zhu, Y.-J. Wang, E. Pineda, T. Wada, H. Kato, J.C. Qiao, Int. J. Eng. Sci. 205 (2024) 104146.
[34] J. Ma, C. Yang, X.D. Liu, B.S. Shang, Q.F. He, F.C. Li, T.Y. Wang, D. Wei, X. Liang, X.Y. Wu, Y.J. Wang, F. Gong, P.F. Guan, W.H. Wang, Y. Yang, Sci. Adv. 5 (2019) eaax7256.
[35] S.K. Huang, F. Sun, W. Ruan, S. Ren, Z. Zhang, X. Liang, J. Ma, J. Mater. Res. Technol. 25 (2023) 2166–2176.
[36] J. Fu, J. Yang, K. Wu, H. Lin, W. Wen, W. Ruan, S. Ren, Z. Zhang, X. Liang, J. Ma, Mater. Horiz. 8 (2021) 1690–1699.
[37] L. Li, X. Li, Z. Huang, J. Huang, Z. Liu, J. Fu, W. Wen, Y. Zhang, S. Huang, S. Ren, J. Ma, Nat. Commun. 14 (2023) 6305.
[38] S. Sohrabi, J. Fu, L. Li, Y. Zhang, X. Li, F. Sun, J. Ma, W.H. Wang, Prog. Mater. Sci. 144 (2024) 101283.
[39] N. Li, W. Chen, L. Liu, JOM 68 (2016) 1246–1261.
[40] J. Ma, J. Yi, D.Q. Zhao, M.X. Pan, W.H. Wang, J. Appl. Phys. 112 (2012) 064505.
[41] J. Fu, Z. Li, X. Li, F. Sun, L. Li, H. Li, J. Zhao, J. Ma, Nano Energy 106 (2023) 108019.
[42] J. Huang, X. Yu, L. Li, W. Wang, H. Zhang, Y. Zhang, J. Zhu, J. Ma, ACS Nano 18 (2024) 2006–2016.
[43] G. Kumar, P.A. Staffier, J. Blawzdziewicz, U.D. Schwarz, J. Schroers, Appl. Phys. Lett. 97 (2010) 101907.
[44] S.-C. Liu, Y.-I. Chen, J.-J. Shyu, H.-Y. Tsai, K.-Y. Lin, Y.-H. Chen, K.-C. Lin, Surf. Coat. Technol. 259 (2014) 352–357.
[45] Y. Zhang, G. Yan, K. You, F. Fang, Surf. Coat. Technol. 391 (2020) 125720.
[46] S. Guo, C.T. Liu, Intermetallics 18 (2010) 2065–2068.
[47] Z. Long, H. Wei, Y. Ding, P. Zhang, G. Xie, A. Inoue, J. Alloys Compd. 475 (2009) 207–219.
[48] K.D. Fischbach, K. Georgiadis, F. Wang, O. Dambon, F. Klocke, Y. Chen, A.Y. Yi, Surf. Coat. Technol. 205 (2010) 312–319.
[49] K. Li, G. Xu, X. Huang, Q. Chen, Z. Xie, F. Gong, Surf. Coat. Technol. 393 (2020) 125839.
[50] K. Bobzin, N. Bagcivan, T. Brögelmann, Mater. Sci. Appl. 05 (2014) 316–329.
[51] Y.-I. Chen, B.-L. Lin, Y.-C. Kuo, J.-C. Huang, L.-C. Chang, Y.-T. Lin, Appl. Surf. Sci. 257 (2011) 6741–6749.
[52] K.C. Chang, H.W. Yang, Y.C. Hsiao, C.C. Chang, F.B. Wu, Surf. Coat. Technol. 205 (2010) 1225–1228.
[53] S.H. Lee, I.H. Ko, T.Y. Kim, Appl. Surf. Sci. 452 (2018) 210–216.
[54] J. Brand, R. Gadow, A. Killinger, Surf. Coat. Technol. 180–181 (2004) 213–217.
[55] K. Li, G. Xu, X. Wen, J. Zhou, F. Gong, Friction 9 (2020) 1648–1659.
[56] F. Bernhardt, K. Georgiadis, L. Dolle, O. Dambon, F. Klocke, Materialwiss. Werkstofftech. 44 (2013) 661–666.
[57] B. Lesiak, J. Zemek, J. Houdkova, A. Kromka, A. Józwik, Anal. Sci. 26 (2010) 217–222.